Environmental Science and Pollution Research (2022) 29:6552–6567
https://doi.org/10.1007/s11356-021-16094-5

RESEARCH ARTICLE

Fabrication of visible light active Mn-doped Bi_2WO_6-GO/MoS_2 heterostructure for enhanced photocatalytic degradation of methylene blue

Noor Tahir[1] · Muhammad Zahid[1] · Ijaz Ahmad Bhatti[1] · Yasir Jamil[2]

Received: 26 April 2021 / Accepted: 18 August 2021 / Published online: 28 August 2021

Abstract

The increase in environmental pollution has led to an increased investigation in the development of novel ternary photocatalytic systems for remediation. These photocatalytic systems exhibit superior photocatalytic action for the removal of pollutants because of their visible light active bandgaps. A highly effective visible light active ternary heterojunction was fabricated using a hydrothermal method assisted by ultrasonication. Herein, we report the in situ hydrothermal synthesis of Mn-doped Bi_2WO_6-GO/ MoS_2 photocatalyst, efficiently exhibiting greater photocatalytic activity for the wastewater treatment under solar light. The binary metal sulphide (MoS_2) used as a co-catalyst, acted as an electron collector and graphene oxide (GO) as a support material for interfacial electron transfer to and from bismuth tungstate and MoS_2. The as-prepared samples were characterized using SEM-EDX, FT-IR, XRD, XPS, BET, PL, and UV–Vis techniques. The bandgap of the novel photocatalyst was found in the visible region (2.2 eV) which helped in suppressing photoinduced electron-hole pairs recombination. The ternary Mn-doped Bi_2WO_6-GO/MoS_2 showed 99% methylene blue removal after 60 minutes of sunlight irradiation at the optimum conditions of pH 8, catalyst dose 50 mg/100ml, and initial MB concentration of 10ppm under sunlight irradiation. The doped ternary heterostructure has proved to be an effective sunlight-active photocatalyst that can be reused without substantial loss in photocatalytic efficiency.

Keywords Heterogeneous photocatalysis; · Wastewater treatment; · Semiconductor metal oxides; · Nanocomposites; · Mn doping; · Graphene oxide

Introduction

Water pollution and energy crisis have become a global threat due to rapid industrialization. Various industries like textile, pharmaceutical, paper, cosmetics, and food industry utilize organic dyes for refining the quality of their manufactured products. These industries frequently produce an extensive load of untreated dye wastewater, making dyes a major component of water pollution (Aziz et al. 2020).

Methylene blue (MB) dye is an immensely used coloring agent for coloring silk, cotton, and wood products. Owing to the complex aromatic structure, the dye methylene blue is resistant to oxidation and degradation by conventionally available methods. Exposure and utilization of water having traces of this dye may cause serious health hazards in humans and animals including nausea, difficult breathing, cyanosis, jaundice, and irritation on the skin and in the eyes. Hence, an appropriate method for the removal of such poisonous dyes is crucial in present times of water shortage (Nawaz et al. 2020). Advanced oxidation processes have received considerable importance because of their role in wastewater treatment and water disinfection. Among Advanced oxidation processes, photocatalysis is considered a green technology because of the utilization of solar energy at ambient conditions (Mushtaq et al. 2020). Heterogeneous photocatalysis is now a promising strategy to address the wastewater crisis owing to the generation of light-induced electrons and holes which can easily scavenge H_2O molecules O_2 and produce reactive oxygen

Responsible Editor: Sami Rtimi

✉ Muhammad Zahid
Zahid595@gmail.com; rmzahid@uaf.edu.pk

[1] Department of Chemistry, University of Agriculture, Faisalabad 38040, Pakistan

[2] Department of Physics, University of Agriculture, Faisalabad 38040, Pakistan

Published online: 28 August 2021

species. Hence, using solar energy one can convert recalcitrant organic pollutants into harmless compounds (Mudhoo et al. 2020). Ternary metal tungstates have been used for water purification owing to their narrow bandgaps, low-cost applicability, crystallinity, and effective utilization of sunlight because of their narrowband gaps (Singh et al. 2020). These ternary compounds suffer from the limitation of high charge carrier recombination. The photocatalytic efficiency of the ternary metal oxides irradiation can be enhanced by coupling with other semiconductor materials having a narrow bandgap and support materials or via doping with transition or plasmonic metals under sunlight (Saher et al. 2021). Since the formation of heterojunctions via coupling and doping both can be effective for suppression of e^-/h^+ recombination by providing new pathways to charge carriers (Mafa et al. 2019). Bismuth tungsten oxide (Bi_2WO_6), is an important member of ternary Aurivillius metal oxides having perovskite layered crystal structure. The sandwich structure consists of alternating layers of $(Bi_2O_2)^{2+}$ and octahedral WO_4^{-2}. This interlayer spacing offers a large surface area and adequate active sites for an efficient photocatalytic process and also prevents electrons and holes from recombining. Bi_2WO_6 (BWO) has a narrow bandgap of (2.80 eV) which makes it efficient as a visible light active photocatalyst as compared to binary compounds (Wang et al. 2017). Although Bi_2WO_6 exhibits excellent photodegradation efficiency towards organic pollutants, its activity is still hindered by some factors including narrow photoresponse limiting maximum utilization of solar light and high recombination rate of charge carriers. Among various approaches being proposed in previous researches, the construction of ternary novel heterojunctions via coupling and doping has widely been used to enhance the charge separation efficiency (Li et al. 2018). Hence, the key step for the formation of novel ternary heterojunctions is the selection of a suitable material for coupling with Bi_2WO_6 ensuring maximum visible light utilization. Among all methods to increase the visible light response of ternary compounds, doping is a relatively effective method. These ternary hybrid photocatalytic systems can separate electrons and holes more efficiently than binary nanocomposites. Doping alters the bandgap and atomic structure of host material by the introduction of foreign ions. The introduction of additional energy levels helps in trapping and separating electrons for a longer period of time hence preventing recombination. Transition metal doping includes use of transition metals like cobalt, niobium, manganese, zinc, tungsten, iron and molybdenum for modifying the d-orbital configuration, the fermi level and the bandgap (Huang et al. 2016). The transition metals have partially filled d orbitals which helps in the formation of new energy bands below the conduction band of host material. These newly formed energy bands are responsible for redshift in the bandgap energy enabling photocatalysts to act efficiently in the visible range of light spectra (Ahmad 2019).

Molybdenum disulfide (MoS_2) is a typical layered two-dimensional layered binary compound particularly used as a hybrid co-catalyst material. A large number of nanocomposites coupled with MoS_2 have been reported which showed enhanced activity because of the existence of S-atoms on exposed ends of MoS_2 (Lv et al. 2017). But the overall photocatalytic reaction activity of MoS_2 alone is reduced due to poor electrical conductivity. Besides the effectiveness of Bi_2WO_6 as a visible light active catalyst and its coupling with MoS_2, a suitable mediator is required for transferring electrons efficiently.

The presence of graphene oxide provides enhanced surface area because of the two-dimensional assembly of carbon atoms which are all Sp^2 hybridized and covalently linked. The high specific surface area of graphene oxide makes it an excellent material for photocatalysis. This is because of facilitation of charge transfer under visible light and attraction for growth of several metal oxides and metals due to the presence of a conjugate system at the basal plane of graphene oxide (Jilani et al. 2018). The electrically conductive large surface area of graphene oxide helps in effective charge migration and acts as a mediator for shuttling electrons between available active sites of photocatalyst and co-catalysts, subsequently suppressing the electrons and holes from reuniting, accelerating the overall catalytic process. Also, graphene oxide adsorbs organic pollutants well on the surface of photocatalysts besides enhancing their photo-response. (Tabasum et al. 2020). Hence, the graphene-supported ternary heterojunctions greatly improve the overall activity of ternary nanocomposites under visible light irradiation.

Herein, we report the synthesis of Mn-doped Bi_2WO_6- supported over graphene oxide and coupled with binary metal sulphide MoS_2 by adjusting the weight percentage of each component in the ternary composite. A simple in situ hydrothermal synthesis process was employed for the fabrication of novel Mn-doped Bi_2WO_6-MoS_2-GO (Mn-BMG) and was employed for the cationic dye methylene blue (MB) degradation under sunlight. The characterization studies of the prepared catalysts were done by techniques like FTIR, SEM-EDX, XPS, XRD, BET, PL, and UV-Vis spectroscopy. The studies showed that graphene oxide-supported Mn-Bi_2WO_6 coupled with MoS_2 provided enhanced surface area and an easy pathway for the transport and separation of photogenerated charge carriers effectively increasing the visible light response of photocatalyst.

Experimental and synthesis

Materials and reagents

Sodium tungstate dihydrate ($Na_2WO_4.2H_2O$, 99% pure), sodium molybdate dihydrate ($Na_2MoO_4{\cdot}2H_2O$, 99%), bismuth

nitrate pentahydrate (Bi $(NO_3)_3.5H_2O$, 97%), sodium nitrate ($NaNO_3$, 98%), potassium permanganate ($KMNO_4$, > 99%), ethylene glycol (analytical grade, 99.8%), sulphuric acid (H_2SO_4, 98%), sodium hydroxide (NaOH pellets, 98%), hydrochloric acid (HCl; 35 % w/w), and hydrogen peroxide (H_2O_2, 35% w/w) were purchased from Sigma Aldrich. Manganese chloride ($MnCl_2.4H_2O$, 98%) was obtained from UNI-Chem reagents. Ethanol (C_2H_5OH; 95.6 % purity) was acquired from Merck. Graphite powder (99%) and thioacetamide (C_2H_5NS, 98%) were obtained from Scharlau. Dye methylene blue (92%) was purchased from Fischer scientific company. All chemicals used were of analytical grade and used without any further purification. Distilled water was used for all the reaction solutions throughout the study.

Synthesis of graphene oxide

Graphene oxide (GO) was synthesized by a modified hummers method. as previously reported in our work (Tabasum et al. 2019). The detailed information is present in the supplementary material.

Synthesis of ternary Mn-BMG

Initially, Bi $(NO_3)_3.5H_2O$ (5mmol) was dissolved in 30ml ethylene glycol (Solution A) and $Na_2WO_4.2H_2O$ (2.5mmol) was dissolved in 30ml distilled water termed Solution B. The prepared solution B was added dropwise in solution A under vigorous stirring. Mn doping (10 mol%) was done by adding precursor $MnCl_2.4H_2O$ (0.0178gm) directly in the above solution and the whole mixture was magnetically stirred for 2 h and poured in a Teflon lined stainless steel autoclave for hydrothermal treatment for 24 h at 180°C temperature. A white powder was obtained after centrifugation and washing thrice with distilled water and ethanol was oven-dried at 60°C. Next, an in situ hydrothermal method was performed in which 2.5mmol of sodium molybdate and 5mmol of thioacetamide were dissolved in 30ml distilled water to form MoS_2 (Solution C). The whole mixture was stirred magnetically for 2 h. The above-prepared Mn-Bi_2WO_6 in 50wt% was dissolved with magnetic stirring in 20 ml distilled water and added dropwise to solution C. Meanwhile, Graphene oxide 20wt% (0.2gm), prepared above was ultrasonically dispersed in 20ml distilled water for about 30 min and added dropwise to Solution C. The whole mixture was vigorously stirred for another 3 h until a homogenous solution was obtained. The whole mixture was again given hydrothermal treatment at 180°C for 24 h by pouring the reaction mixture in a 250-ml capacity autoclave. The prepared black powder was centrifuged, washed thrice using distilled water and ethanol, and dried in an electric oven at 60°C for 12 h. The undoped ternary Bi_2WO_6-MoS_2-GO (BMG) was prepared by a similar method except for the addition of $MnCl_2.4H_2O$. The binary BW-GO (BG) was prepared by a method reported earlier by Nguyen and his fellows (Nguyen et al. 2018).

Characterization and equipment

The microstructure, morphology, and elemental analysis of as prepared ternary Mn-BMG and BMG were characterized using a scanning electron microscope equipped with EDX (SEM-EDX; FEI NOVA 450 NANOSEM). The crystalline properties of all powder samples were measured by XRD (Bruker D8 Advancedequipment operated) over a range of 2θ values from 5 to 85 degrees. The presence of several functional groups on the surface of prepared photocatalysts was studied by Fourier transform infrared spectroscopy (FTIR, Thermo Nicolet). The XPS analysis was done to study the elemental states and the surface chemical compositions investigated (Escalab 250 XPS system, Thermo Fisher Scientific UK). The surface area and surface porosity of the as-synthesized composites were analyzed using a Brunauer–Emmett–Teller (BET) surface analyzer (Nova 2200e Quantachrome). The photoluminescence spectra of all the composites were studied using Shimadzu RF-5301PC, spectro-fluorophotometer, and the excitation wavelength for PL analysis was 325 nm for all samples. The bandgap analysis of the ternary doped and undoped samples was done using UV–VIS spectrophotometer (Cecil CE 7200) in the 200–800 nm range by dispersing catalysts in water under ultrasonication.

Evaluation of photocatalytic degradation

Various experiments on the photocatalytic degradation of cationic dye methylene blue (MB) were carried out under sunlight in batch mode using ternary Mn-BMG, BMG, and binary BG nanocomposites for 1 h. The nanocomposites in different concentrations were initially screened in Ultraviolet and Visible irradiation to check the feasibility of the MB degradation. The effect of several parameters including pH (2–9), catalyst dosage (10–100mg/100ml), initial dye concentration (2–20 ppm), and irradiation time (10–120 min) on MB photodegradation was studied. For comparison, a single experiment was performed under UV irradiation for each catalyst at their optimum conditions. The control experiments of dye/sunlight, Dye/UV, Dye/UV light/catalyst were also run to examine the dye removal under these conditions also. For the photocatalytic degradation of MB under sunlight, the desired quantities of catalysts were dispersed via ultrasonication in 100 mL of 10 ppm dye solution. Before exposing the solutions to sunlight, the solutions were stirred mechanically in dark to obtain adsorption-desorption equilibrium for nearly thirty minutes. Before exposure to any light source, the adsorption capacity of samples was examined. After checking the adsorption capacity of photocatalysts, the dye solutions were kept

under sunlight irradiation for about 60 min at 180 rpm in electrical orbital shakers. After each trial, the nanocomposites were separated from the solution by centrifugation of 5ml dye solution and the concentration of the remaining dye was determined by taking absorbance of clear solution using a UV–VIS spectrophotometer at 665nm. A blank beaker of dye solution was also kept in dark and sunlight to investigate dye degradation in the presence and absence of light. The % degradation was calculated using the following formula

$$\%\text{Degradation} = 1-\frac{A}{Ao} \times 100 \quad (1)$$

Here, Ao is the initial absorbance and A is absorbance after treatment under solar light. The pH was maintained by using different molar concentration solutions of HCl and NaOH using a pH meter (Ohaus ST3100, USA). The sunlight intensity was measured by a solar power meter (SM206), and the brightness was measured by a light meter (HS1010A). The reusability of catalysts was investigated by 5 times recycling the catalysts and reusing them at optimum conditions under sunlight each time with freshly prepared 10 ppm MB solution.

Characterization

FTIR analysis

FTIR analysis was employed to elucidate the existence of several functional groups and chemical bond formation in the Mn-doped and undoped ternary BMG samples as shown in (Fig. 1). Transmittance peaks were observed around 645 cm^{-1}, 948 cm^{-1}, 1024 cm^{-1}, 1069 cm^{-1}, 1380 cm^{-1}, 1450 cm^{-1}, and 1620 cm^{-1} for the ternary nanocomposites. The peaks at around 1024 cm^{-1} and 1069 cm^{-1} have appeared because of O=S=O asymmetric stretching vibrations and S-O-S symmetric vibrations, respectively. Additionally, the presence of a peak at 1185 cm^{-1} shows asymmetric vibrations of Mo-O bonds confirming the synthesis of MoS_2 as described in previous studies (Zolgharnein and Rastgordani 2018). An elongated broad band from 645 to 845 cm^{-1} is accredited to Bi–O and W–O stretching vibrations. A peak at 715.46 cm^{-1} explains the antisymmetric bridging mode which is associated with tungstate chains. An intense peak present at 1384 cm^{-1} explains the bending vibrations of W–O–W. These characteristic bands of BW were observed for all samples. (Khojeh et al. 2017). The absorption band appearing at 1450 cm^{-1}, 1557.9 $cm^{-1,}$ and 1630.75 cm^{-1} indicates the formation of COO^{-}, C=C, and C=O stretching vibrations indicating successful fabrication of GO and incorporation of GO into BW (Hu et al. 2019). The skeletal vibrations of graphene sheets appearing at 1630.75 cm^{-1} indicate carbonyl stretching that the oxygen-comprising groups in GO are decomposed upon exposure to a hydrothermal environment. But no other obvious absorption peak related to GO could be observed in the composites due to the low content of GO (Liu et al. 2017). These vibrations appearing at 1630cm^{-1} may also indicate adsorbed water molecules and unoxidized graphitic domains (Hou et al. 2020) A very small peak is visible at 947 cm^{-1} in Mn-doped ternary composite as compared to undoped ternary sample, which is ascribed to Mn-O vibrations as confirmed from previous studies (Ahmad et al. 2019). Besides, the peak intensity is reduced in the doped ternary composite, which supports the successful insertion of dopant ions into the host material.

XRD analysis

The phase purity and crystalline structures of all the ternary and binary samples were studied by XRD characterization in the 2θ range of 5–85° as shown in (Fig. 2). The influence of manganese doping and GO/MoS_2 coupling on the crystalline structure of bismuth tungstate were also affirmed through XRD. All the strong diffraction peaks of Bi_2WO_6 are readily indexed at 2θ values 28.02°, 32.8°, 47.12° and 55.7°, well assigned to (131), (200), (260), and (331) crystal planes indicating the successful formation of Bi_2WO_6 in orthorhombic phase (JCPDS card, No. 73-1126). The sharp diffraction peaks of bismuth tungstate in all samples including Mn-BMG, BMG, and BG are the same showing formation of high purity and crystalline single-phase orthorhombic bismuth tungstate, showing that the addition of MoS_2 and GO has not affected the orthorhombic structure of bismuth tungstate. The peaks at 2θ values of 39.2° and 52.2° corresponding to (100) and (110) planes, indicating the formation of amorphous molybdenum disulphide (JCPDS 37–1492). No other visible peaks of MoS_2 are observed suggesting low crystallinity and trace loading of MoS_2 on the GO support. The reported peak of graphene oxide at 10 disappears and appears at 23.5° indexed (002), exhibiting that the graphene oxide is a highly oxidized product. No extra visible peaks of graphene oxide could be detected in all the XRD patterns owing to the less content and stacking of GO in the ternary nanocomposite, (Zhou et al. 2019). The fewer XRD patterns of GO in ternary hybrids show stacking of GO and its function as a substrate for nucleation and growth of MoS_2 upon exposure to hydrothermal treatment (Li et al. 2015). The absence of any impurity peak in the Mn-BMG sample infers the effective substitution of divalent cations (Mn^{2+}) in the bismuth tungstate matrix. The peaks in the XRD pattern of Mn-doped samples are lower in intensity as compared to the undoped ternary composite sample. Additionally, a peak shift to higher diffraction angles position has also been observed in the Mn-doped sample as compared to the undoped sample suggesting that the Mn^{2+} ions successfully doped the host ternary composite. This peak shift suggests changes in interstitial Bi_2WO_6 unit cell volume

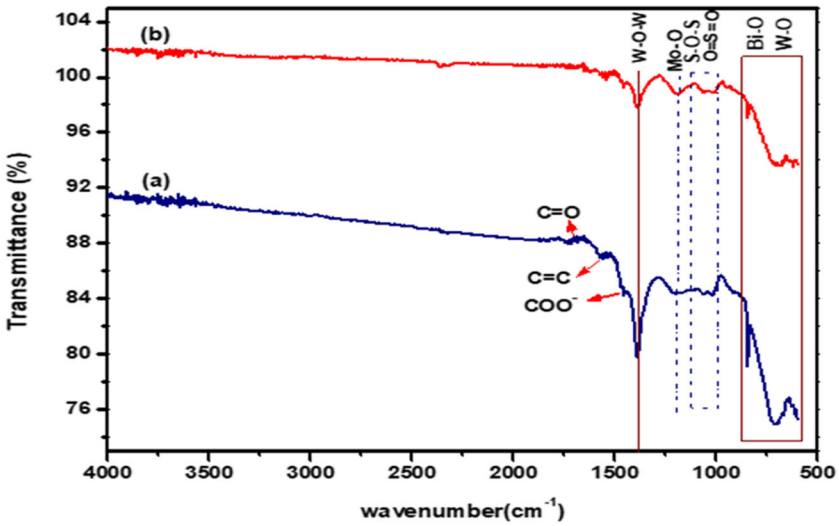

Fig. 1 FTIR spectra of (a) BMG and (b) Mn-BMG ternary nanocomposites

as a result of doping. The ionic radius of Bi^{+2} ions is larger than that of Mn^{2+}ions, hence Mn^{2+} ions can enter Bi_2WO_6 host lattice and substitute Bi^{+2} ions, causing the XRD pattern to shift to higher diffraction angles (inset of Fig. 2) Similar outcomes of Mn doping in host lattice were also observed by Reddy et al (Reddy et al. 2019). Ahsaine and co-workers observed the systematic broadenings of Bragg peaks in the XRD patterns of upon dopping of Bi_2WO_6 samples (Ahsaine et al. 2016a). The average particle size was calculated using Debye-Scherrer formulae equation 3:

$$D = 0.9\lambda/\beta cos\theta \quad (2)$$

D is the particle size, λ is the wavelength of CuKα (i.e., 0.154 nm), β explains the intensity at full-width half maximum of diffraction line which is expressed in radians, and θ refers to Bragg's angle. The average particle size of BMG and Mn-BMG particles was found to be 15.2 nm and 14.44 nm respectively. The smaller crystallite size of Mn-doped nanocomposite can be referred to as the better growth of nanoparticles onto support media but having restricted dimensions which may distort host lattice due to insertion of Mn^{+2} ions decreasing nucleation and grain growth (Chanu et al. 2019).

SEM analysis

The morphology and microstructure of as-synthesized pristine and doped samples were investigated by Scanning electron microscope (SEM) at various resolutions. SEM images determined the morphological changes after doping in the surface of the ternary nanocomposite. After combining Mn-Bi_2WO_6 with MoS_2 and GO the ternary hybrid showed a hierarchical

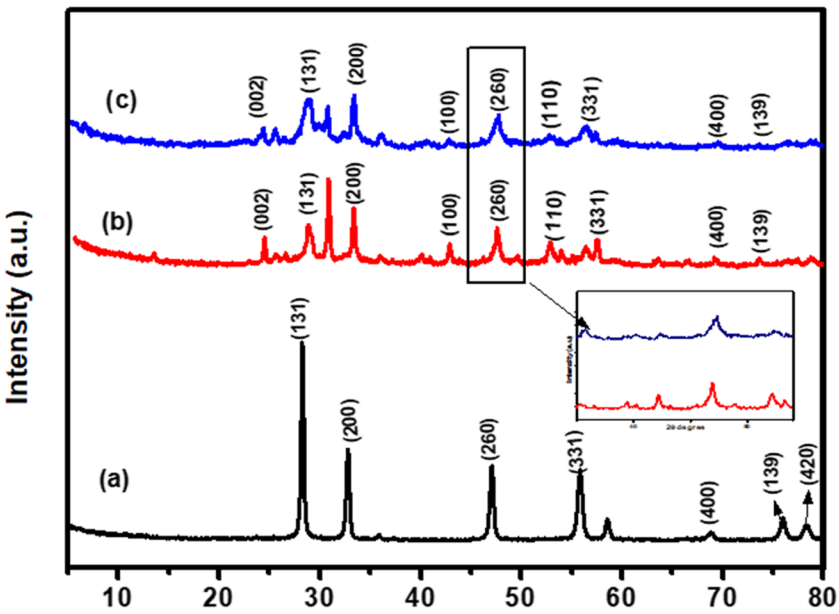

Fig. 2 X-ray diffraction patterns of (a) BG, (b) BMG, and (c) Mn-BMG nanocomposites

structure showing the assembly of plenty of bismuth tungstate nanorods interlaced and flower-like nanostructured MoS_2 distributed over stacked graphene sheets Fig. 3(c). The MoS_2 exhibited nanoflowers-like morphology as in Fig 3. (a) and are clearly shown growing on the edges alongside stacking of graphene oxide ternary heterostructure of SEM images Fig. 3 (b). The undoped ternary composite exhibited severe agglomeration due to the stacking of graphene oxide. The exterior coarse texture of nanoplates is because of coverage and stacking of GO sheets However, this agglomeration notably weekend after the introduction of Mn in the nanocomposite. This suggests that Mn doping effectively suppressed the severe aggregation of particles (Dou et al. 2020). The Mn-doped Bi_2WO_6-graphene shows uniformed surface nanorods and less agglomeration. The ternary doped nanocomposite with all the components present, well separated with minimized aggregation, uniform structure, and Mn particles uniformly attached to Bi_2WO_6 rods Fig. 3 (c &d). Hence, the incorporation of Mn in the host lattice influenced the morphology of the particles.

EDX analysis

EDX elemental mapping confirmed the chemical configuration and distribution of Bi, W, C, S, N, O according to their nominal weight percentages as shown in Fig. 4. The undoped ternary BMG did not show the presence of any impurity atom whereas the EDX pattern of doped ternary hybrid shows Mn atom in 1.68 wt% which is also confirmed by the XPS spectra, suggesting successful incorporation of Mn in ternary nanocomposite according to their nominal chemical stoichiometry amounts. It also confirms the presence of all other elements including Bi, W, O, C, Mo, S, and Na. Little changes in the wt% of all elements are observed after the hydrothermal processing.

XPS analysis

The composition and chemical states of all the elements present and the interactions among all the three components in the ternary nanocomposite are analyzed by XPS spectra. The elemental composition of BMG and Mn-BMG was investigated through XPS survey scan which revealed the peaks of Bi (165.06eV), W(37.61eV), O1s (534.82eV), S2p (163 eV), C1s (284.17eV), and Mn as shown in Fig. 5a while the atomic percentage of detected elements were shown in Fig. 5(b). The Bi 4f peak appearing at a binding energy of 165.067eV ascribed to $Bi4f_7$ and $Bi4f_5$ Bi^{+3} ions in Bi_2WO_6 nanoparticles. The O1s peak in the ternary component at a binding energy of 536.0eV is assigned to the metal-oxygen bonds of Bi_2WO_6 and also to the adsorbed water molecules on the catalyst's

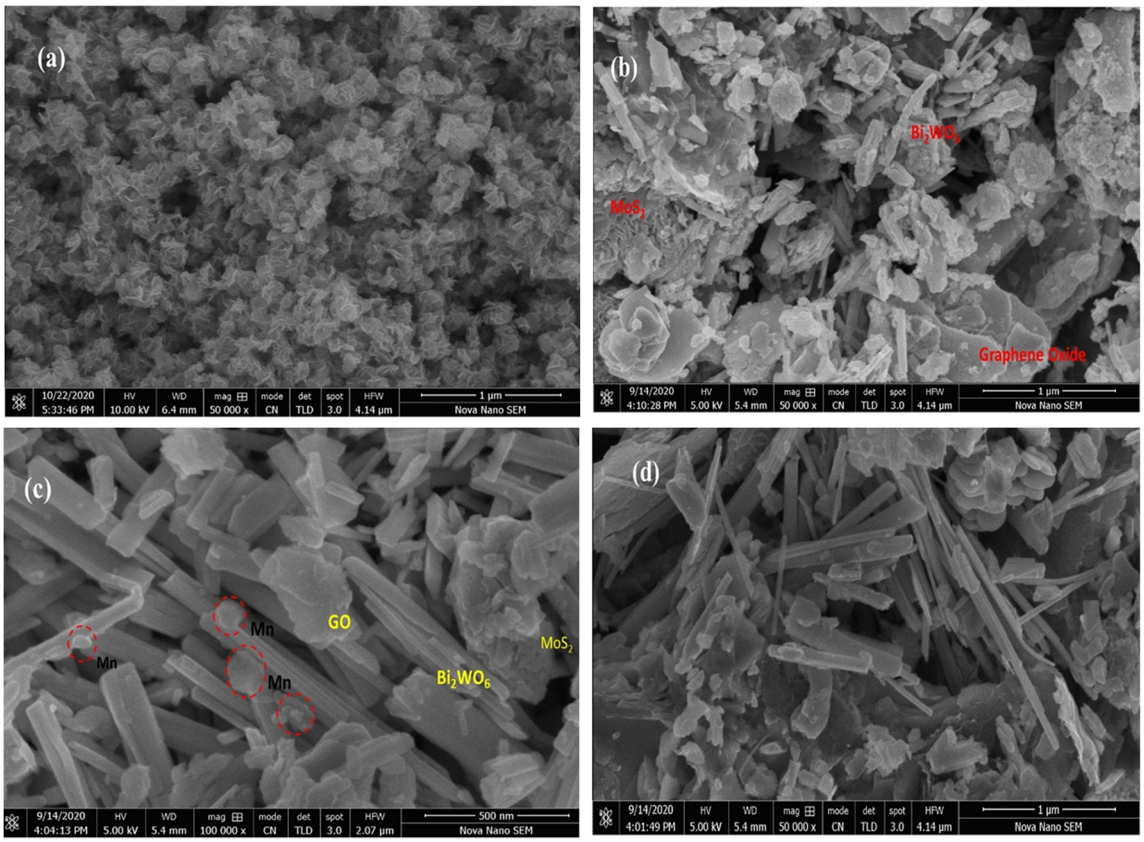

Fig. 3 SEM images of (a) MoS_2 nanoflowers, (b) BMG, (c &d) Mn-BMG

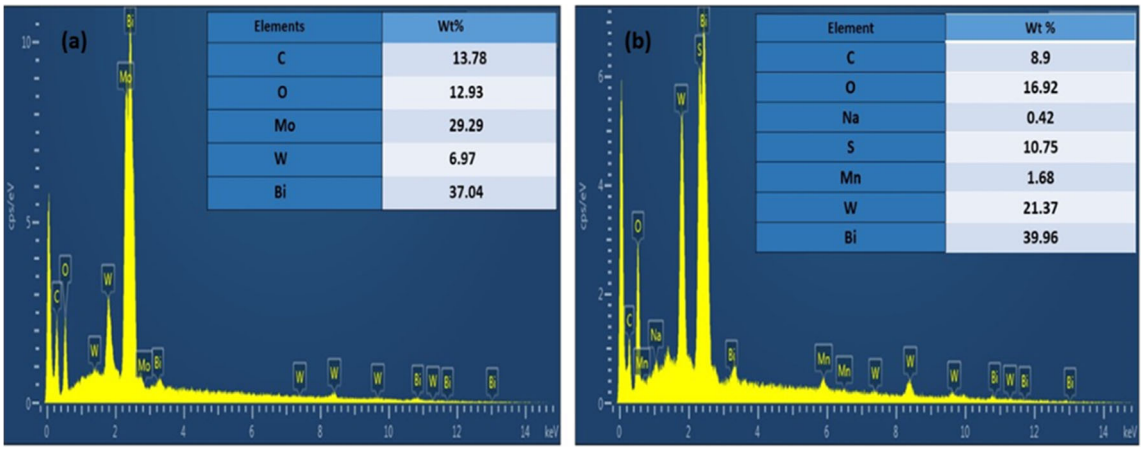

Fig. 4 EDX spectra of (a)BMG (b) Mn- BMG ternary nanocomposites

surface (Ahsaine et al. 2018). The C1s peak at 284.17 eV is possibly credited to the adventitious residual carbon as also confirmed from previous studies (Yang et al. 2015). In the C1s spectra, peaks appearing at 284.7eV and 285.4 eV are assigned to the sp^2 and sp^3 hybridization of carbon atoms while the peak at 289.5 eV is assigned to the C=O bond (Jilani et al. 2020). A peak appearing at a binding energy of 1011eV is assigned to Mn^{2+}, respectively, indicating the presence of Mn^{+2}. Characteristic deconvoluted peaks appearing at 640.04eV and 649.27eV are ascribed to $Mn2p_{3/2}$ and $Mn2p_{1/2}$, respectively. Thus, XPS data confirms the presence of Mn ions in doped ternary nanocomposite (Dou et al. 2020). The high-resolution XPS of Wf_4 shows two peaks detected at 37.81eV and 34.30 eV suggesting $W4f_{5/2}$ and $W4f_{7/2}$ of W_{6+}. oxidation state. The peak at 163 eV is the S2p peak matched exactly well with the S^{2-} binding energy which is required for MoS_2 formation (Singha et al. 2020). Also, the peak at 229 confirms dominant presence of Mo^{4+} species in the high-resolution XPS spectra The small pair of peaks arising towards the higher binding site at about 232.36eV and 229 eV corresponds to Mo $3d_{3/2}$ and Mo $3d_{5/2}$, signifying conversion of Mo^{4+} to Mo^{6+} as consistent with previous studies (Fig. S1) (Senthil et al. 2019). The peaks appearing at 162.83eV matches well with Bi $4f_{5/2}$ and Bi $4f_{7/2}$ and are allotted to the Bi^{3+} oxidation state of Bi_2WO_6 in both ternary samples. The characteristic peaks of W4f, Bi4f, C1s, and O1s in Mn-BMG ternary nanocomposite show a shift towards higher binding energies in comparison with the undoped ternary sample. This may be due to change in certain electronic interactions between all three components as a result of Mn doping (Dong et al. 2017). The results show the coexistence of various oxidation states $Mn^{3+,}$ $Mn^{4+}$and Mn^{2+} linked to (Mn-O), at various binding energy positions present on the sample's surface. The deconvolution of Bi4f, C1s, Mn2p3, Mo3d, O1s, S2p and, W4f XPS peaks are shown in fig. S1 of supplementary data. The atomic percentage of S2p, O1s, C1s,

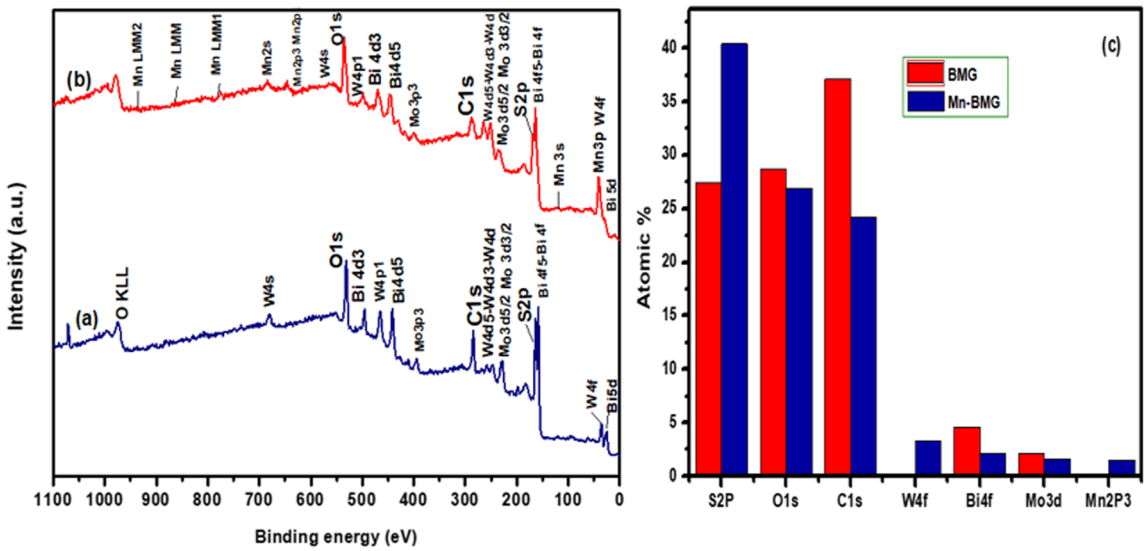

Fig. 5 XPS survey spectrum of (a) BMG, (b) Mn-BMG, and (c) atomic percentages of BMG and Mn-BMG

W4f, Bi4f, Mo3d, Mn2p3 is 40.4%, 26.9%, 24.2%, 3.3%, 2.1%, 1.6%, and 1.5% respectively in Mn-BMG, while the undoped counterpart comprised of C1s, O1s, S2p, Bi4f, Mo3d, W4f in 37.1%, 28.7%, 27,4%, 4.6%, 2.1%, and 0.2% atomic percentages respectively.

BET surface area analysis

The surface area of photocatalysts is a crucial factor for determining the photodegradation efficiency of photocatalysts. A large surface area provides an enhanced surface for the attachment of pollutant molecules and resultantly a large number of radicals can react and degrade them effectively. To explore the surface characteristics such as specific surface area, pore-volume, and pore size, nitrogen (at 77 K) adsorption-desorption experiments were performed on the surface of ternary photocatalysts (BMG and Mn-BMG). The adsorption isotherms are shown in Fig. S2 (a & b) of supplementary material. Both the Adsorption isotherms are categorized as type IV isotherms according to the IUPAC classification, with an obvious hysteresis loop. This loop is a characteristic of mesoporous materials and lamellar pore structures. The specific surface area was calculated using the BET (Brunauer-Emmett-Teller) method from the adsorption data of nitrogen gas and is found to be 6.630 m^2/g for BMG, and the specific surface area of Mn-BMG is 9.624 m^2/g owing to the doped Mn ions. It can be observed that doping has increased the specific surface area besides changing the morphology of doped photocatalyst, ultimately enhancing the photodegradation efficiency (Ahsaine et al. 2016b). Moreover, the pore size distribution curves Fig. S2 (c& d) demonstrates that both nanocomposites exhibit hierarchical pore structure with pore size distribution ranging from 2 to 20 nm. The enhanced surface area of Mn-BMG was owing to reduced size of the photocatalyst. As the size of the photocatalyst reduced, the surface area increased (Tahir et al. 2021). A comparison of surface area, pore-volume, and pore diameter are shown in Table 1.

Photoluminescence analysis

The recombination efficiency of photogenerated electrons and holes during the photocatalytic reaction is evaluated by Photoluminescence spectroscopy. The efficiency of any photocatalyst is determined by its ability to separate e^-/h^+ pairs proficiently. The recombination rate of e^-/h^+ pairs is directly proportional to the PL intensity The Photoluminescence properties of all the composites are shown in Fig. 6. The most intense peak is of binary BG composite revealing that more emissions occur as a result of more recombination of light-generated charge carriers. The peaks positioned at 365 nm and 468 nm arise due to the interstitial effect caused by the Mn doping (Keerthana et al. 2021). A decline in photoemission and peak intensity in the ternary Mn-BMG sample confirmed the suppression of recombination of electrons and holes, consequently leading to an enhancement in photocatalytic activity. The PL of Mn-doped BMG shows less intensity as compared with all other composites. The luminescent peak in Mn-BMG is suppressed due to doping with Mn ions, which may overwhelm the oxygen vacancies present in the crystal lattice (Reddy et al. 2019). The Mn-BMG has a narrow optical bandgap as compared to Bi_2WO_6-GO and BMG that helps in retaining the recombination of generated charge carriers. The PL spectra intensity is also directly linked to the charge recombination ratio. The weaker PL intensity in Mn-BMG shows a decline in charge recombination ratio due to addition of graphene oxide support and Mn ions. Furthermore, in comparison with BG and BMG, PL peaks shifted for Mn-BMG, possibly owing to the interaction among functional groups such as carbonyl of Graphene oxide and Bi_2WO_6 interstitials. This interaction may also lead to the creation of some surface defects, that might provide active sites for the attachment of pollutants (Jilani et al. 2021). Hence, as compared with binary composite and undoped ternary composite, the Mn-doped ternary BMG exhibited higher photocatalytic degradation efficiency due to suppression in recombination of charge carriers.

Optical analysis

The optical response was measured by observing UV-VIS absorption spectra and determine the bandgap energies of pure and Mn-doped ternary nanocomposite in the range of 200–900nm. The absorption edge of the Mn-doped BMG nanocomposite was found in the visible region using the tauc plot as shown in Fig. 7. The Mn-doped BMG showed an even greater range of light absorption to the entire visible spectrum in comparison to the pristine ternary sample. The Mn doping in ternary heterojunctions improved the optical absorption

Table 1 Summary of Surface area, pore-volume, and pore diameter of pure and Mn-doped BMG nanoparticles

Photocatalysts	Surface area (m^2/g)	Pore volume (cm^3/g)	Pore diameter(nm)
BMG	6.630	0.029	11.687 nm
Mn-BMG	9.624	0.047	12.225nm

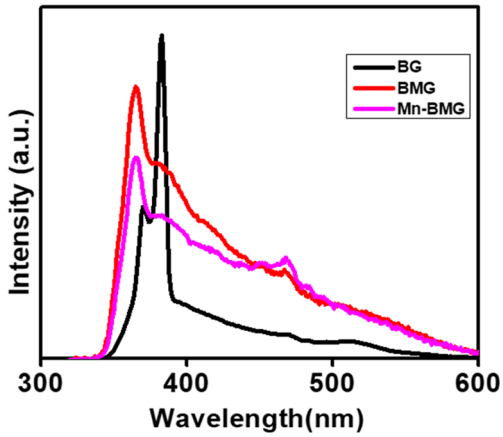

Fig. 6 Photoluminescence spectra of BG, BMG, and Mn-BMG

providing a possibility to enhance photo-induced electron-hole pairs generation ultimately enhancing the photodegradation in the visible region. The bandgap energies of the catalysts were estimated using the formula given in equation 4.

$$(\alpha hv)2 = B\,(hv - Eg) \tag{3}$$

where Eg =hν when αhν = 0 and the $(\alpha h\nu)^2$ is plotted against energy in eV. The absorption energy is taken at hν value where it then extrapolates to α=0 as shown in Fig. 5. The estimated band gap energies were found to be 2.4 eV and 2.2 eV for BMG and Mn-BMG. Here, α B, and ν are described as the absorption coefficient, proportionality constant, and the light frequency. The optical studies show that all the photocatalysts show strong absorption in the visible light region.

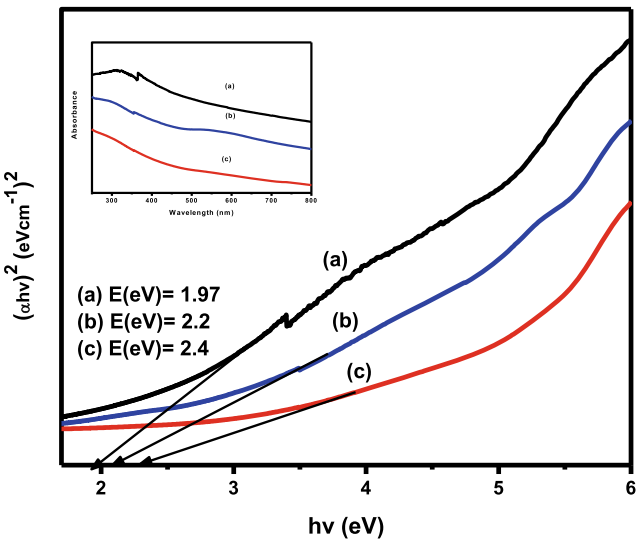

Fig. 7 Bandgap energies estimation of (a) BG and (b) Mn-BMG (c) BMG by Tauc plot method with inset showing the UV-VIS absorption spectra of the BMG and Mn-BMG

Effect of operational parameters

Effect of pH

In the photodegradation process, the key factor that directly affects the photoefficiency of the photocatalytic system is the pH of the aqueous solution. The pH governs the surface charge characteristics of the photocatalysts according to their point of zero charges (pH_{PZC}) and also the adsorption capacity of the organic molecules on the surface of the catalyst (Ahmadi et al. 2020). The effect of pH on the photodegradation of MB was examined by changing pH values from 2 to 9 keeping all other factors constant (catalyst dose=50 mg/100mL for doped and undoped ternary and 40mg/100ml for binary BG, Initial dye concentration: 10ppm, and irradiation time 60 min). The pH of dye solutions was maintained using 0.1 M and 1mM solutions of sodium hydroxide hydrochloric acid. Methylene blue is a cationic dye hence it is positively charged upon dissociation in water. The pH_{PZC} value for Mn-BMG was determined at pH 6.2. At pH values lower than the pH_{PZC}, the surface of the catalyst is positively charged and the positively charged MB dye molecules are electrostatically repulsed. In the acidic medium, the active sites on the catalyst's surface are weak to produce hydroxyl radicals, consequently decreasing the dye degradation (Nie et al. 2014). At pH values above 6.2, the catalyst's surface is negatively charged and the cationic MB dye molecules were electrostatically attracted towards the catalyst surface, enhancing the adsorptive property of dye molecules. The active sites on the surface of the catalyst showed increased hydroxyl radicals production resulting in the increased MB degradation in the basic medium. Hence, the ternary Mn-BMG showed 99% photocatalytic degradation in an alkaline medium at optimum pH of 8 under visible light irradiation of 60 minutes as shown in Fig. 8(a). The undoped ternary BMG at pH 8 and binary BG at pH 7 showed 95% and 92% degradation respectively in the presence of sunlight for about the same time duration.

Effect of catalyst dose

The amount of catalyst used is another important parameter for the evaluation of photocatalytic performance and economic cost. To understand the relation among catalyst loading and photodegradation efficiency, degradation of 10ppm MB dye solution was investigated in the range of 10–80mg/100mL, keeping all others factors constant (pH=8) for Mn-doped and undoped ternary,7 for binary BG, catalyst dose= optimum of each catalyst, and irradiation time 60 min. Photocatalyst doses ranging from 10mg–100mg/L were used to study the influence on degradation. The photodegradation efficiency of Mn-BMG was enhanced from 69 to 99% as the catalyst dose was increased from 10 to 50mg. The increase in catalyst dose

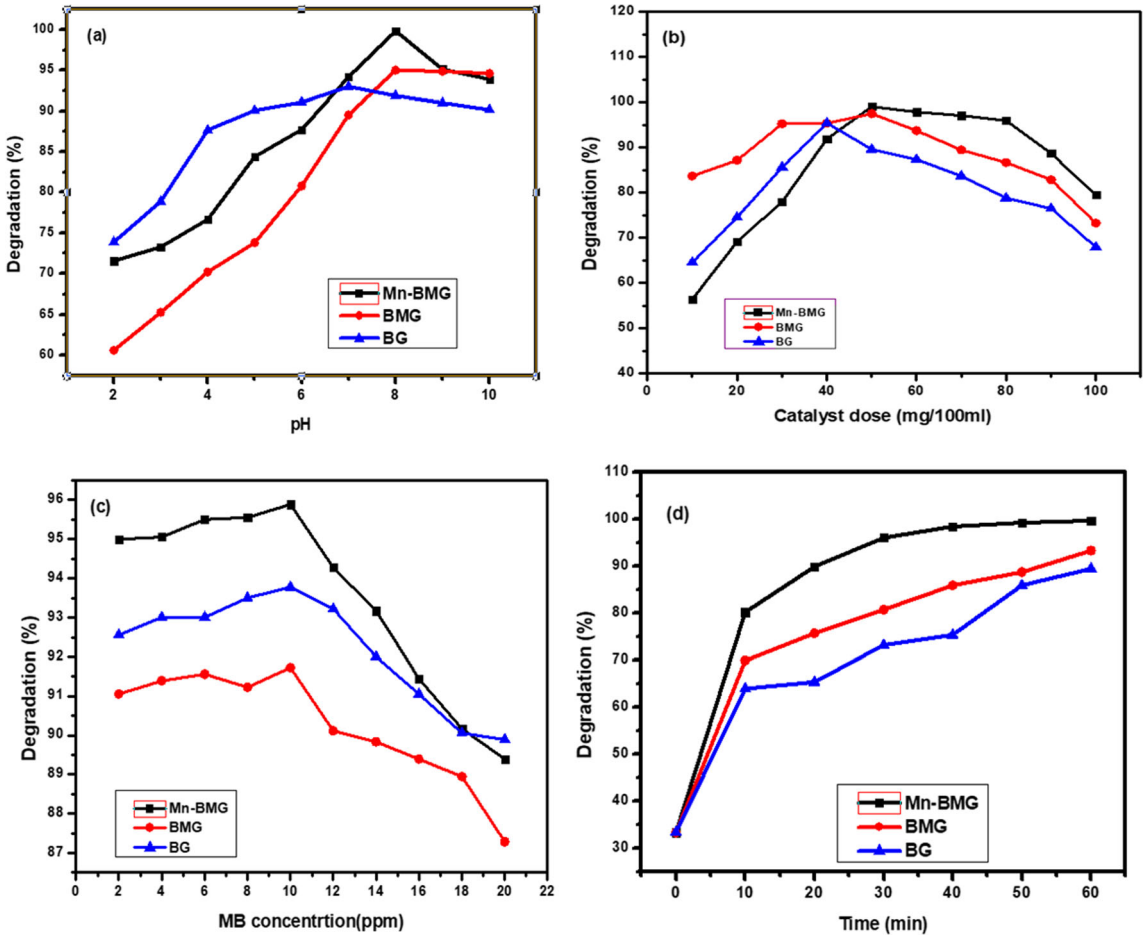

Fig. 8 Optimization of reaction parameters using Mn-BMG, BMG, and BG (a) pH, (b) catalyst dose, (c) Initial dye concentration (d) Irradiation time

enhances the number of active sites on the catalyst's surface, consequently enhancing the production of hydroxyl and superoxide radicals. The undoped and doped ternary composites showed enhanced photodegradation at an optimum catalyst dose of 50mg/ml and binary BW-GO at 40mg/100ml as shown in graph b of Fig. 8 (b). An increase in catalyst dose above 50 mg showed a slight increase up to 97% and started decreasing when it went beyond 100mg. This reduction in degradation is owing to the interception of light preventing light photons to reach the surface of adsorbed contaminants because of agglomeration of catalysts at their higher doses and subsequent unavailability of active sites (Hu et al. 2019). Hence, catalyst dose decides the limits of a catalyst for particular organic pollutants in wastewater above which the rate of degradation eventually decreases. Graphene oxide-supported composites prevent agglomeration and show effective degradation even at higher concentrations (Tabasum et al. 2021).

Effect of initial dye concentration

The dye degradation is highly dependent upon the concentration of dye adsorbed on the catalyst surface. The effect of initial dye concentrations ranging from 2 to 20ppm was studied for the photodegradation of MB by Mn-BMG and all other nanocomposites keeping all other factors constant at their optimal values. At initial low MB load, maximum degradation was attained which is linked to the availability of maximum active sites and also due to the reaction between dye molecules and hydroxyl radicals formed on the catalyst's surface. As the dye concentration is increased, active sites on the catalyst surface become saturated as more dye molecules are adsorbed on the surface. The number of photons reaching the surface of the catalyst becomes fewer causing less generation of hydroxyl radicals for effective degradation of MB molecules (Nawaz et al. 2020). The performance of all photocatalysts is shown in graph c of Fig. 8. All catalysts showed maximum degradation at a methylene blue concentration of 10ppm. The ternary Mn-BMG nanocomposite showed above 90% degradation even at higher MB concentrations. This is because the ternary heterojunction has enhanced surface area and can adsorb enhanced concentration of MB molecules. The vacant active sites available after the degradation of adsorbed dye molecules on the surface of the photocatalyst are rapidly occupied by other dye molecules near the catalyst surface (Mushtaq et al.

2020). This results in enhanced MB degradation even at higher dye loads by the novel Mn-BMG as compared to other photocatalysts

Effect of irradiation time

The maximum energy that is required for the initiation of photocatalytic reaction comes directly from the light energy hence, the conditions of light illumination have a great impact on the overall performance of photocatalysts. Fig shows the decomposition efficiency of MB over Mn-BMG, BMG, and BG under sunlight irradiation. Under the optimum conditions for all catalysts, The dye solutions were exposed to light irradiation for various for about an hour. The UV-VIS absorption spectra of treated MB solutions after irradiation under sunlight were recorded in the 400–800nm range each after ten minutes. The spectral changes in the treated dye solution were observed by plotting absorbance data as a function of time. The trends show an increase in the degradation as time increases as shown in Fig. S3 (a, b, c for BMG, Mn-BMG, and BG) of supplementary information. The dye color starting disappearing right after 30 min of irradiation and complete degradation was observed around 60 min of irradiation using novel Mn-BMG whereas, the decrease in the intensity was gradual with time using ternary BMG and binary BG. The rapid decrease in intensity upon light irradiation is signifying that chromophore groups responsible for imparting colour are breaking down slowly. Furthermore, the kinetic models are applied to this data.

Kinetics of photodegradation reaction

Two kinetic models first-order and second-order were studied for the photodegradation of dye methylene blue by the doped and undoped ternary nanocomposites. The expression for each model is expressed in equations 3-4

First-order kinetics:

$$ln\frac{\mathrm{Co}}{\mathrm{Ct}} = k_1 t \tag{3}$$

Second-order kinetics:

$$\frac{1}{Ct} - \frac{1}{Co} = k_2 t \tag{4}$$

Figure 9 (b) shows a linear relationship between ln(Co/Ct) and reaction time, where Co and C are the initial concentrations, indicating that the photodegradation of methylene blue by doped and undoped ternary nanocomposites follows first-order kinetics. The plot of Co/Ct versus time represents a straight line where the slope of which upon linear regression equals the apparent first-order rate constant k. The higher rate constants k of Mn-BMG for the first-order reaction than undoped ternary indicates that Mn-doped composite is more effective under sunlight than undoped BMG composite. The values of R^2 for the first-order reaction for doped and undoped ternary composites are 0.9967 and 0.993 respectively, suggesting that the ternary hybrids effectively follow the first-order reaction. The rate constant k of the doped component is more than that of undoped ternary revealing that doping has caused an acceleration in the degradation rate under visible light A. The higher rate constant of doped BMG than other photocatalysts explains that the Mn-BMG shows more photoefficiency than others. Comparison of correlation coefficients for a first order and second order are shown in Table 2.

Type of the photocatalyst and the role of dopant species

The type of photocatalyst used is the most imperative parameter for greater photocatalytic degradation. The bandgap, crystallinity, porosity, surface area, and nature of dopant all determine the effectiveness of catalyst in the visible light region (Aydoghmish et al. 2019). Among all principal approaches, transition metal doping in semiconductor heterostructures is the most practical way to activate them under visible light, thus reducing the distance between the valence band and conduction band. Various chemical and surface modifications occur including porosity and enhanced surface area because of the introduction of a suitable dopant species in the photocatalyst structure, increasing the photocatalytic efficiency (Akerdi and Bahrami 2019). The ternary nanocomposites as compared to binary composites show increased degradation due to the synchronized activation of the charge transfer mechanism between the various semiconductor materials. The transfer of charges between the conduction bands of two metal oxides and a support material leads to enhanced charge separation and less agglomeration by increasing the specific surface area ultimately offering more active sites. The ternary undoped BMG showed 94% degradation in visible light as compared to the binary counterpart.

The addition of dopant species in the semiconductor ternary system further improved the photocatalytic activity which is mainly ascribed to alteration in the bandgap energy, following the transfer of energy. The addition of dopant creates additional energy levels and leading to better separation and transfer of photogenerated charge carriers to the surface of the catalyst. This separation mainly depends upon two factors including large surface area and the light absorbed by the catalyst (Aydoghmish et al. 2019). Therefore, the doped ternary Mn-BMG showed strong visible light region absorption and greater degradation for methylene blue up to 99.7% in 1 h.

Table 2 Correlation coefficients (R^2) and kinetic parameters for MB (Co=10ppm) degradation

Photocatalysts	Experimental conditions			First-order kinetics		Second-order kinetics	
	pH	Photocatalyst dose(mg/L)	Initial dye concentration(ppm)	$k1(min^1)$	R^2	$K2$ ($L\mu mol^1 min^1$)	R^2
Mn-BMG	8	50mg	10ppm	0.0866	0.9967	0.43215	0.729
BMG	8	50mg	10ppm	0.02899	0.993	0.14207	0.8616
BW	7	40mg	10ppm	0.0255	0.987	0.0886	0.8487

Degradation under UV irradiation

A sole experiment was done in UV radiations considering the optimized conditions specific for all the photocatalysts. Methylene blue was degraded almost completely in UV irradiation only after exposure of half an hour by Mn-BMG. Undoped BMG and binary BG also performed well under ultraviolet light and their ternary heterojunction has shown more than 90% degradation under UV light. Similar results of greater MB degradation by ternary nanocomposite were shown earlier in UV light degradation (Aydoghmish et al. 2019).

Radical scavenging and proposed mechanism

The determination of active species involved in the photocatalytic process is significant for understanding the degradation mechanism of organic pollutants. In the degradation of dyes, several active radical species such as hydroxyl radicals (OH·), holes, (h^+), electron (e−) superoxide anion radical ($\cdot O^{-2}$) play a vital role (Rajendran et al. 2018). Hence, to investigate the key active species involved during the photocatalytic process, a radical scavenging experiment was performed. 5mM of EDTA (ethylene-diamine-tetra-acetate), $K_2Cr_2O_7$ (potassium dichromate), DMSO (dimethyl sulfoxide) were used to scavenge holes, electrons, and hydroxyl radicals. The experiment was performed under sunlight. From Fig. 11 (a), it is clear that EDTA is the main radical scavenger in the degradation process of MB dye by Mn-BMG, as the addition of EDTA decreased the degradation values from 99 to 48.83. The addition of DMSO decreased the degradation from 99 to 55% indicating that hydroxyl radicals also have a contributing role in addition to holes. Very little change was observed by the addition of $K_2Cr_2O_7$ indicating that electrons do not play a major role in MB degradation by Mn-Bi_2WO_6-GO/MoS_2.

The proposed mechanism of MB degradation by Mn-BMG, suggests that holes and hydroxyl radicals are the main active species. Holes are directly responsible for degradation and producing more hydroxyl radicals. Upon sunlight irradiation, both Bi_2WO_6 and MoS_2 are excited and produce electrons and holes. The photoexcited electrons get transferred from the conduction band of MoS_2 having a negative potential towards the conduction band of Bi_2WO_6 having a positive potential. While the photoinduced holes accumulate above the valence band of MoS_2. The reactive holes accumulated on the surface of MoS_2 directly oxidize MB dye molecules adsorbed on the catalyst surface. Graphene oxide has a large

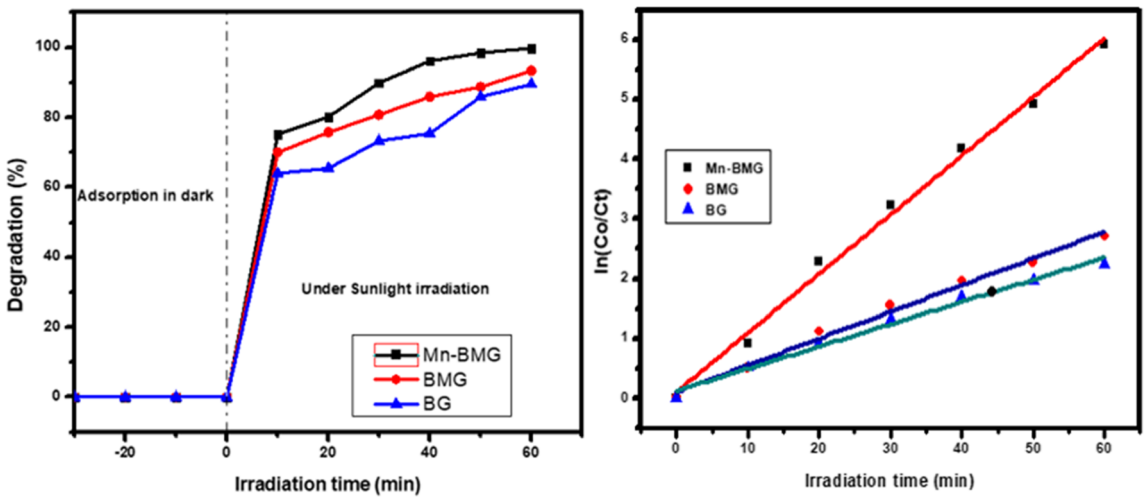

Fig. 9 MB % removal as a function of time (a) photocatalytic degradation of MB in the presence of sunlight, catalysts under optimum conditions. (a) First-order kinetic model fitting

Table 3 Comparison between various bismuth tungstate-based ternary heterostructures for methylene blue degradation

Sr.No	Photocatalyst	Synthesis Method	Model pollutant	Light source	Irradiation time (min)	Degradation (%)	Reference
1.	Bi_2WO_6-CdS-PVA	Hydrothermal method	MB	Visible light	100	92%	(Rajendran et al. 2018)
2.	$Bi_2WO_6/MoSe_2$-$Bi_{12}O_{17}C_{l0.5}Br_{1.5}$	Hydrothermal synthesis	MB	Visible light	60	99.7%	(Tahir et al. 2021)
3.	$Ag_8W_4O_{16}/AgBiW_2O_8/Bi_2WO_6$	Green double displacement method	MB	UV light	40	82.5%	(Mendoza-Mendoza et al. 2020)
4.	Ag@AgBr-Bi_2WO_6	oil-in-water self-assembly method.	MB	Visible light	120	95.03%	(Lin et al. 2015)
5.	Fe-Bi_2WO_6-$BiVO_4$	Hydrothermal	MB	Visible light	120	90%	(Chaiwichian et al. 2016)
6.	Bi_2WO_6/TiO_2/polyester	Hydrothermal	MB	Visible light	150	95.1%	(Du et al. 2018)
7.	Cu_2O/Bi_2WO_6	Interfacial-self assembly method	MB	Visible light	120	98.6	(Liu et al. 2016)
8.	Lu-Bi_2WO_6	Co-precipitation method	MB	Visible light	120	99.3%	(Ahsaine et al. 2016b)
9.	Fe_3O_4-Bi_2WO_6-GS	Hydrothermal method	MB	Visible light	210	98.2%	(Wang et al. 2019)
10.	Bi_2WO_6/MnO_2	Template free method	MB	Visible light	100	99%	(Salari and Yaghmaei 2020)
11.	N/Ti^{3+}-TiO_2/Bi_2WO_6	Hydrothermal method	MB	Visible light	50	96%	(Sun et al. 2020)
12.	Mn-Bi_2WO_6-GO-MoS_2	Hydrothermal method	MB	Visible light	60	99%	This work

surface area and electrical conductivity acts as a mediator and transfers electrons to and from MoS_2 and Bi_2WO_6. Mn doping introduces additional energy levels in Bi_2WO_6, hence photo-induced electrons and holes take longer to recombine. Eventually, the photo-response of the ternary heterojunction is increased towards visible light. A similar mechanism has been proposed by lv et al., (Lv et al. 2017). Hence, holes are responsible for the degradation of dyes and production of hydroxyl radicals whereas, the influence of electrons and superoxide anions is relatively less. Figure 10 shows the degradation mechanism by ternary Mn-BMG. Table 3 shows a comparison of various Bismuth tungstate nanocomposites for degradation of dye methylene blue.

Reusability

Under the optimized conditions for each photocatalyst, the stability of catalysts was confirmed by using the catalysts repeatedly in five successive trials. For this, the catalysts are

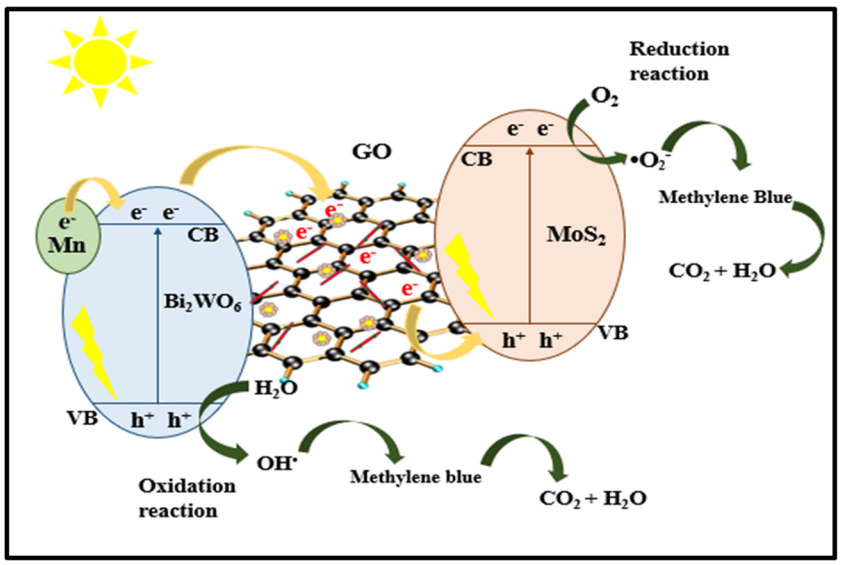

Fig. 10 Photocatalytic degradation mechanism of Dye Methylene blue by Mn-BMG

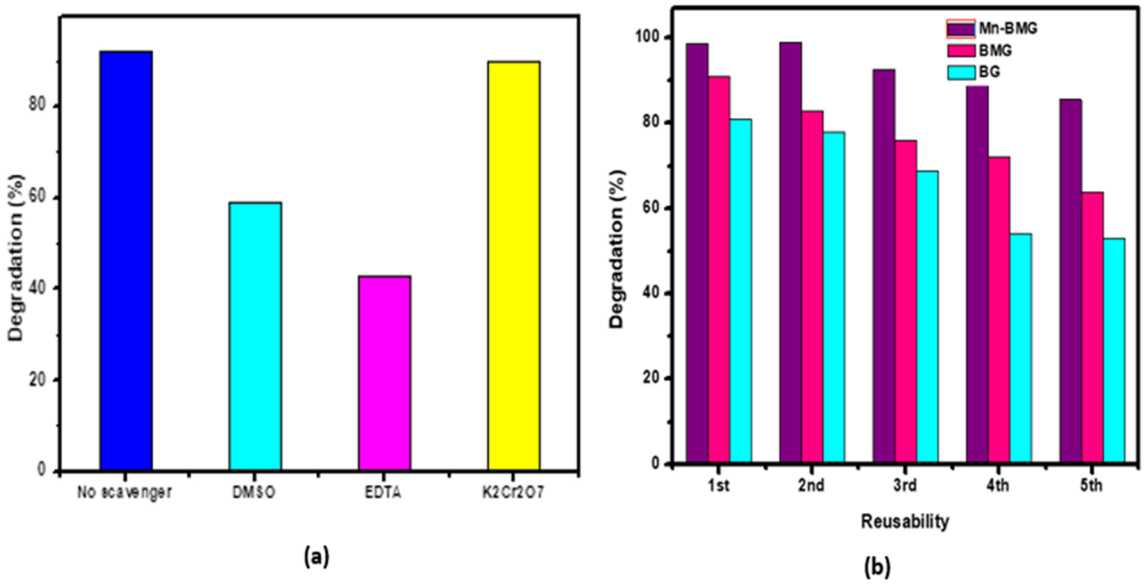

Fig. 11 (a) Study of various radical scavengers, (b) reusability of Mn-BMG, BMG, BG nanocomposites

separated from the treated MB dye solution by centrifugation then rinsed thrice using distilled water and later dried up at 60°C in an electric oven. The catalysts are then weighed and investigated for their photocatalytic efficiency. All the reusability trials are run at the same optimized conditions for each catalyst, i.e. at pH 8, catalyst dose- 50mg/100m, IDC 10ppm for doped undoped ternary nanocomposite, and pH 7, catalyst dose 40mg/100ml, IDC 10ppm for binary BG. No substantial loss in photocatalytic activity was observed after five runs with just a 10% decrease in catalytic activity Fig. 11 (b). The results revealed that the ternary-doped composite exhibits high mechanical stability and reusability.

Conclusion

The novel ternary hybrid Mn-BMG has found valuable applications for Organic pollutants degradation. The doped ternary photocatalyst was synthesized by an in situ hydrothermal method. The ternary hybrid showed excellent degradation for dye methylene blue under sunlight irradiation. Undoped ternary BMG and binary BG were also prepared to compare the degradation efficiencies of doped and undoped ternary hybrids with binary composite. The Mn-BMG showed 99% MB degradation in an hour. The improved photocatalytic efficiency was credited to the ternary heterojunction formed as a result of Bi_2WO_6, MoS_2, and GO. The ternary heterojunction has the characteristics of all three components and the Mn doping further suppresses the electron-holes recombination. The photostability of photocatalysts was evaluated by five consecutive runs with less than a 10% reduction in degradation.

Supplementary Information The online version contains supplementary material available at https://doi.org/10.1007/s11356-021-16094-5.

Author contribution Noor Tahir: Data curation, visualization, investigation, writing—original draft, writing—review & editing. Muhammad Zahid: conceptualization, project administration, resources, supervision, writing—review & editing. Ijaz Ahmad Bhatti: conceptualization, methodology, software, writing—review & editing. Yasir Jamil: visualization, investigation, validation.

Funding This research was funded by the Higher Education Commission (HEC), Pakistan, under Indigenous 5000 Ph.D. Fellowship with student PIN "pin # 518-121977-2PS5-032 (50043428)".

Data availability The datasets used and/or analyzed in this study are available in the manuscript and supplementary information additional information can be asked from the corresponding author upon request.

Declarations

Ethics approval and consent to participate Not applicable

Consent for publication All the authors agree to publish this article.

Competing interest The authors declare no competing interests.

References

Ahmad I (2019) Inexpensive and quick photocatalytic activity of rare earth (Er, Yb) co-doped ZnO nanoparticles for degradation of methyl orange dye. Sep Purif Technol 227:115–126

Ahmad M, Khan MY, Sadaf S, Iqbal S, Nawaz F, Iqbal J (2019) Novel indigo-dye-doped graphene-supported Mn/WO_3 nanocomposite as visible light photocatalyst for degradation of methylene blue dye. Mater Res Express 6:055050

Ahmadi S, Rahdar A, Igwegbe CA, Mortazavi-Derazkola S, Banach AM, Rahdar S, Singh AK, Rodriguez-Couto S, Kyzas GZ (2020) Praseodymium-doped cadmium tungstate ($CdWO_4$) nanoparticles for dye degradation with sonocatalytic process. Polyhedron 190: 114792

Ahsaine HA, Ezahri M, Benlhachemi A, Bakiz B, Villain S, Guinneton F, Gavarri JR (2016a) Novel Lu-doped Bi2WO6 nanosheets: Synthesis, growth mechanisms and enhanced photocatalytic activity under UV-light irradiation. Ceram Int 42:8552–8558

Ahsaine HA, Slassi A, Ezahri M, Benlhachemi A, Bakiz B, Guinneton F, Gavarri J-R (2016b) Electronic band structure and visible-light photocatalytic activity of Bi_2WO_6: elucidating the effect of lutetium doping. RSC Adv 6:101105–101114

Ahsaine HA, Slassi A, Naciri Y, Chennah A, Jaramillo-Páez C, Anfar Z, Zbair M, Benlhachemi A, Navío JA (2018) Photo/electrocatalytic properties of nanocrystalline ZnO and La–Doped ZnO: Combined DFT fundamental semiconducting properties and experimental study. ChemistrySelect 3:7778–7791

Akerdi AG, Bahrami SH (2019) Application of heterogeneous nano-semiconductors for photocatalytic advanced oxidation of organic compounds: a review. J Environ Chem Eng 7:103283

Aydoghmish SM, Hassanzadeh-Tabrizi S, Saffar-Teluri A (2019) Facile synthesis and investigation of NiO–ZnO–Ag nanocomposites as efficient photocatalysts for degradation of methylene blue dye. Ceram Int 45:14934–14942

Aziz A, Ali N, Khan A, Bilal M, Malik S, Ali N, Khan H (2020) Chitosan-zinc sulfide nanoparticles, characterization and their photocatalytic degradation efficiency for azo dyes. Int J Biol Macromol 153:502–512

Chaiwichian S, Wetchakun K, Phanichphant S, Kangwansupamonkon W, Wetchakun N (2016) The effect of iron doping on the photocatalytic activity of a Bi_2WO_6–$BiVO_4$ composite. RSC Adv 6:54060–54068

Chanu LA, Singh WJ, Singh KJ, Devi KN (2019) Effect of operational parameters on the photocatalytic degradation of Methylene blue dye solution using manganese doped ZnO nanoparticles. Results Phys 12:1230–1237

Dong S, Ding X, Guo T, Yue X, Han X, Sun J (2017) Self-assembled hollow sphere shaped Bi_2WO_6/RGO composites for efficient sunlight-driven photocatalytic degradation of organic pollutants. Chem Eng J 316:778–789

Dou R, Cheng H, Ma J, Komarneni S (2020) Manganese doped magnetic cobalt ferrite nanoparticles for dye degradation via a novel heterogeneous chemical catalysis. Mater Chem Phys 240:122–181

Du Z, Cheng C, Tan L, Lan J, Jiang S, Zhao L, Guo R (2018) Enhanced photocatalytic activity of Bi_2WO_6/TiO_2 composite coated polyester fabric under visible light irradiation. Appl Surf Sci 435:626–634

Hou X, Wang Z, Fan G, Ji H, Yi S, Li T, Wang Y, Zhang Z, Yuan L, Zhang R (2020) Hierarchical three-dimensional MoS_2/GO hybrid nanostructures for triethylamine-sensing applications with high sensitivity and selectivity. Sensors Actuators B Chem 317:128–236

Hu K, Chen C, Zhu Y, Zeng G, Huang B, Chen W, Liu S, Lei C, Li B, Yang Y (2019) Ternary Z-scheme heterojunction of Bi_2WO_6 with reduced graphene oxide (rGO) and meso-tetra (4-carboxyphenyl) porphyrin (TCPP) for enhanced visible-light photocatalysis. J Colloid Interface Sci 540:115–125

Huang F, Yan A, Zhao H (2016) Influences of doping on photocatalytic properties of TiO_2 photocatalyst. In: Wenbin C (ed) Semiconductor photocatalysis-materials, mechanisms and applications. IntechOpen, London, pp 31–80

Jilani A, Othman MHD, Ansari MO, Hussain SZ, Ismail AF, Khan IU (2018) Graphene and its derivatives: synthesis, modifications, and applications in wastewater treatment. Environ Chem Lett 16:1301–1323

Jilani A, Rehman GU, Ansari MO, Othman MHD, Hussain SZ, Dustgeer MR, Darwesh R (2020) Sulfonated polyaniline-encapsulated graphene@ graphitic carbon nitride nanocomposites for significantly enhanced photocatalytic degradation of phenol: a mechanistic study. New J Chem 44:19570–19580

Jilani A, Hussain SZ, Ansari MO, Kumar R, Dustgeer MR, Othman MHD, Barakat M, Melaibari AA (2021) Facile synthesis of silver decorated reduced graphene oxide@ zinc oxide as ternary nanocomposite: an efficient photocatalyst for the enhanced degradation of organic dye under UV–visible light. J Mater Sci 56:7434–7450

Keerthana S, Yuvakkumar R, Ravi G, Mustafa AE-ZM, Al-Ghamdi AA, Elshikh MS, Velauthapillai D (2021) PVP influence on Mn–CdS for efficient photocatalytic activity. Chemosphere 277:130346

Khojeh B, Zanjanchi M, Golmojdeh H (2017) Preparation of catalytically active bismuth tungstate: effects of organic additives and dopants. Mater Res Innov 21:341–349

Li F, Zhang L, Li J, Lin X, Li X, Fang Y, Huang J, Li W, Tian M, Jin J (2015) Synthesis of Cu–MoS_2/rGO hybrid as non-noble metal electrocatalysts for the hydrogen evolution reaction. J Power Sources 292:15–22

Li B, Lai C, Zeng G, Qin L, Yi H, Huang D, Zhou C, Liu X, Cheng M, Xu P (2018) Facile hydrothermal synthesis of Z-scheme $Bi_2Fe_4O_9$/Bi_2WO_6 heterojunction photocatalyst with enhanced visible light photocatalytic activity. ACS Appl Mater Interfaces 10:18824–18836

Lin S, Liu L, Hu J, Liang Y, Cui W (2015) Nano Ag@ AgBr surface-sensitized Bi_2WO_6 photocatalyst: oil-in-water synthesis and enhanced photocatalytic degradation. Appl Surf Sci 324:20–29

Liu L, Ding L, Liu Y, An W, Lin S, Liang Y, Cui W (2016) Enhanced visible light photocatalytic activity by Cu_2O-coupled flower-like Bi_2WO_6 structures. Appl Surf Sci 364:505–515

Liu M, Xue X, Yu S, Wang X, Hu X, Tian H, Chen H, Zheng W (2017) Improving photocatalytic performance from Bi_2WO_6@ MoS_2/graphene hybrids via gradual charge transferred pathway. Sci Rep 7:1–11

Lv H, Liu Y, Tang H, Zhang P, Wang J (2017) Synergetic effect of MoS_2 and graphene as cocatalysts for enhanced photocatalytic activity of $BiPO_4$ nanoparticles. Appl Surf Sci 425:100–106

Mafa PJ, Ntsendwana B, Mamba BB, Kuvarega AT (2019) Visible light driven $ZnMoO_4$/$BiFeWO_6$/rGO Z-scheme photocatalyst for the degradation of anthraquinonic dye. J Phys Chem C 123:20605–20616

Mendoza-Mendoza E, Nuñez-Briones A, Ysiwata-Rivera A, Moral-Rodríguez A, García-Cerda L, Peralta-Rodríguez R, Rodríguez-Hernández J, Rodríguez-López J (2020) Novel Silver and Bismuth Tungstate-Based Nanostructures Synthesized by a Green Route and Their Application to Dye Photodegradation. Water Air Soil Pollut 231:1–15

Mudhoo A, Paliya S, Goswami P, Singh M, Lofrano G, Carotenuto M, Carraturo F, Libralato G, Guida M, Usman M (2020) Fabrication, functionalization and performance of doped photocatalysts for dye degradation and mineralization: a review. Environ Chem Lett 18: 1825–1903

Mushtaq F, Zahid M, Mansha A, Bhatti I, Mustafa G, Nasir S, Yaseen M (2020) $MnFe_2O_4$/coal fly ash nanocomposite: a novel sunlight-active magnetic photocatalyst for dye degradation. Int J Environ Sci Technol 17:4233–4248

Nawaz A, Khan A, Ali N, Ali N, Bilal M (2020) Fabrication and characterization of new ternary ferrites-chitosan nanocomposite for solar-light driven photocatalytic degradation of a model textile dye. Environ Technol Innov 20:79–100

Nguyen DCT, Cho KY, Jung C-H, Oh W-C (2018) Photocatalytic activities of contaminants by Bi_2WO_6-graphene composites decorated with mesoporous silica. J Alloys Compd 766:477–487

Nie M, Yang Y, Zhang Z, Yan C, Wang X, Li H, Dong W (2014) Degradation of chloramphenicol by thermally activated persulfate in aqueous solution. Chem Eng J 246:373–382

Rajendran R, Varadharajan K, Jayaraman V, Singaram B, Jeyaram J (2018) Photocatalytic degradation of metronidazole and methylene blue by PVA-assisted Bi_2WO_6–CdS nanocomposite film under visible light irradiation. Appl Nanosci 8:61–78

Reddy CV, Reddy IN, Akkinepally B, Harish V, Reddy KR, Jaesool S (2019) Mn-doped ZrO_2 nanoparticles prepared by a template-free method for electrochemical energy storage and abatement of dye degradation. Ceram Int 45:15298–15306

Saher R, Hanif M, Mansha A, Javed H, Zahid M, Nadeem N, Mustafa G, Shaheen A, Riaz O (2021) Sunlight-driven photocatalytic degradation of rhodamine B dye by $Ag/FeWO_4/gC_3N_4$ composites. Int J Environ Sci Technol 18:927–938

Salari H, Yaghmaei H (2020) Z-scheme 3D Bi_2WO_6/MnO_2 heterojunction for increased photoinduced charge separation and enhanced photocatalytic activity. Appl Surf Sci 532:147413

Senthil RA, Osman S, Pan J, Sun Y, Kumar TR, Manikandan A (2019) A facile hydrothermal synthesis of visible-light responsive $BiFeWO_6$/MoS_2 composite as superior photocatalyst for degradation of organic pollutants. Ceram Int 45:18683–18690

Singh P, Shandilya P, Raizada P, Sudhaik A, Rahmani-Sani A, Hosseini-Bandegharaei A (2020) Review on various strategies for enhancing photocatalytic activity of graphene based nanocomposites for water purification. Arab J Chem 13:3498–3520

Singha SS, Rudra S, Mondal S, Pradhan M, Nayak AK, Satpati B, Pal P, Das K, Singha A (2020) Mn incorporated MoS_2 nanoflowers: A high performance electrode material for symmetric supercapacitor. Electrochim Acta 338:135815

Sun M, Yao Y, Ding W, Anandan S (2020) N/Ti^{3+} co-doping biphasic TiO_2/Bi_2WO_6 heterojunctions: hydrothermal fabrication and sonophotocatalytic degradation of organic pollutants. J Alloys Compd 820:153172

Tabasum A, Zahid M, Bhatti HN, Asghar M (2019) Fe_3O_4-GO composite as efficient heterogeneous photo-Fenton's catalyst to degrade pesticides. Mater Res Express 6:015608

Tabasum A, Bhatti IA, Nadeem N, Zahid M, Rehan ZA, Hussain T, Jilani A (2020) Degradation of acetamiprid using graphene-oxide-based metal (Mn and Ni) ferrites as Fenton-like photocatalysts. Water Sci Technol 81:178–189

Tabasum A, Alghuthaymi M, Qazi UY, Shahid I, Abbas Q, Javaid R, Nadeem N, Zahid M (2021) UV-Accelerated Photocatalytic Degradation of Pesticide over Magnetite and Cobalt Ferrite Decorated Graphene Oxide Composite. Plants 10:1–6

Tahir MB, Nawaz T, Alrobei H, Shahzad K, Muhammad S (2021) Construction of $Bi_2WO_6/MoSe_2/Bi_{12}O_{17}ClxBr^{2-}$ x heterostructures for the production of hydrogen energy and degradation of methylene blue. Appl Nanosci 11:951–959

Wang J, Tang L, Zeng G, Liu Y, Zhou Y, Deng Y, Wang J, Peng B (2017) Plasmonic Bi metal deposition and $g\text{-}C_3N_4$ coating on Bi_2WO_6 microspheres for efficient visible-light photocatalysis. ACS Sustain Chem Eng 5:1062–1072

Wang F, Zhang J, Jia D, Ma Y, Ma L, Lu G (2019) Flower-like structured Fe_3O_4− MQDs/Bi_2WO_6/GNs heterojunction with high-efficiently charge transfer for organic contaminants degradation. J Taiwan Inst Chem Eng 99:276–283

Yang J, Wang X, Zhao X, Dai J, Mo S (2015) Synthesis of uniform Bi_2WO_6-reduced graphene oxide nanocomposites with significantly enhanced photocatalytic reduction activity. J Phys Chem C 119: 3068–3078

Zhou H, Liu Y, Zhang L, Li H, Liu H, Li W (2019) Transition metal-doped amorphous molybdenum sulfide/graphene ternary cocatalysts for excellent photocatalytic hydrogen evolution: Synergistic effect of transition metal and graphene. J Colloid Interface Sci 533:287–296

Zolgharnein J, Rastgordani M (2018) Multivariate optimization and characterization of simultaneous removal of binary mixture of Cu (II) and Pb (II) using Fe_3O_4@MoS_2 nanoparticles. J Chemom 32:30–43